Proceedings of the ASME 2023 Heat Transfer Summer Conference
HT2023
July 10-12, 2023, Washington, DC

HT2023-107426

EXPERIMENTAL ANALYSIS OF SINGLE EVAPORATION TUBE UTILIZING SINTERED COPPER PARTICLE WICKING STRUCTURES

Jeremy Spitzenberger
Multiphysics Energy Research Center, University of Missouri
Columbia, MO

James Hoelle
Multiphysics Energy Research Center, University of Missouri
Columbia, MO

Ramy H. Mohammed
Multiphysics Energy Research Center, University of Missouri
Columbia, MO

Laith Ismael
Multiphysics Energy Research Center, University of Missouri
Columbia, MO

Hongbin Ma
Multiphysics Energy Research Center, University of Missouri
Columbia, MO

Pengtao Wang
Building Technologies Research and Integration Center (BTRIC), Oak Ridge National Laboratory
Oak Ridge, TN

Stephen Kowalski
Building Technologies Research and Integration Center (BTRIC), Oak Ridge National Laboratory
Oak Ridge, TN

Kashif Nawaz
Building Technologies Research and Integration Center (BTRIC), Oak Ridge National Laboratory
Oak Ridge, TN

ABSTRACT

Wicking structures have been widely used within passive heat transfer devices with high heat fluxes, such as heat pipes, to enhance their thermal performance. While wicking structures promote capillary pumping of the working fluid as well as thin film evaporation, they can result in capillary evaporation and further enhances the evaporation heat transfer. In this study, a 0.5 mm thick layer of 105 μm sintered copper particles was added to the inner wall of a copper tube, aiming to enhance the heat transfer characteristics by taking advantage of capillary evaporation. Acetone was chosen as the working fluid, and the performance of an evaporation tube was tested for power inputs of 10, 30, 50, and 70 W. For each power input, trials were run at inclination angle varying from -90° and 90° to investigate the capillary effects. The temperature measurements showed that the temperature distribution along the evaporation tube is always downward sloping, meaning the temperature at the fluid inlet is larger than the outlet. Interestingly, the surface temperature at some locations is less than the outlet temperature, indicating the effect of capillary evaporation. In addition, a theoretical investigation was performed to investigate the effects of the particle size on the thermal performance of the evaporation tube and found that particle sizes affect capillary evaporation.

Keywords: copper sintered particles, evaporation, heat transfer

1. INTRODUCTION

Passive heat transfer devices have gained serious traction in recent years due to their ability to transfer heat extremely efficiently. Improving passive heat transfer in devices such as heat pipes has been at the forefront of research today. A current topic of interest is the effect that wicking structures have on the heat transport capability in passive heat transfer systems. Wicking structures have long been implemented within heat pipes to return working fluid to the evaporating section but utilizing wicking structures to enhance capillary evaporation can greatly improve evaporative heat transfer coefficients and critical heat fluxes. Bigham et al. [1] noted that the main method used to enhance capillary evaporation effects for flow boiling is the introduction of a wicking structure and that wicking structures can have many shapes and geometries. Introducing a wicking structure serves three main purposes: improving thin film evaporation, liquid rewetting of the inner tube surface, and bubble nucleation and growth.

Bigham and Moghaddem [2,3] introduced a novel way to measure heat transfer events of flow boiling in a microchannel due to bubble generation from wicking structures. The experimental studies deconstruct the boiling heat transfer process into basic heat transfer mechanisms, confirming bubble growth contributes to thin film evaporation in the overall heat transfer of the device. Palko et al. [4] experimentally studied the effects of a porous copper microchannel in conjunction with micromachined heat sinks for high heat flux (>1 kW/cm^2)

applications in electronics. It was determined the porous copper structure enhanced the evaporative heat transfer due to improved thin film evaporation on the wicking structure. Plawsky et al. [5] compiled results and conclusions from the 2013 International Workshop on Micro- and Nanostructures for Phase-Change Heat Transfer on thin-film evaporation. It was concluded that thin film evaporation enhances many heat transfer processes, which include energy conversion, microelectronics cooling, boiling, perspiration, and self-assembly operations. It was also noted that surface topography, i.e., wicking structures, can drastically enhance vaporization processes and therefore heat transfer capability of the device.

Thome [6] conducted a comprehensive literature review on the boiling mechanisms within a microchannel. The compiled analytical and experimental results show that the dominant heat transfer mechanism is evaporating thin films around elongated bubbles. Results showed that macroscale models do not represent the heat transfer mechanisms properly, but should rather focus on the transient thin film evaporation. Liquid rewetting in microchannels is crucial in ensuring thin film evaporation at the elongated bubbles. Xu et al. [7] experimentally measured the effects of the rewetting process within a microchannel. As the microchannel became partially or completely dried out, the heat transfer capability of the device significantly decreased. By rewetting the device, bubble nucleation occurred, which promoted thin film evaporation, and the overall heat transfer ability of the device was improved. Wang et al. [8] experimentally showed that liquid rewetting of the microchannel induced bubble nucleation, growth, and coalescence, which prompted transient flow and enhanced heat transfer. Dupont et al. [9] proposed a heat transfer model describing the heat transfer capability of a liquid slug, an evaporating elongated bubble, and a vapor slug. The model supports that heat transfer is enhanced due to the evaporating thin film and the importance of proper rewetting to prevent dryout and, thus, the loss of the evaporating thin film. Kandlikar et al. [10] proposed a flow boiling configuration with open microchannels and either a uniform or tapered manifold. The presence of the manifold produced more surfaces for bubble nucleation while reducing backflow due to bubble nucleation and preventing bubble nucleation from drying out areas on the heated surface which led to a dramatic improvement in heat transfer performance.

Dai et al. [11] developed a micromembrane using a single layer of a sintered copper mesh screen to enhance capillary evaporation. The group experimentally determined that the addition of the micromembrane enhanced the evaporating surface and improved the critical heat flux by 83% and 198% when compared to microchannels and copper woven mesh laminates, respectively, under similar design and operating conditions. Zhang et al. [12] conducted a visualization study on phase change within a gravity-capillary evaporation microgrooved heat pipe. It was found that the corner-film evaporation occurring in the rectangular microgrooves improves the overall phase change evaporation performance. Wang et al. [13] applied an aluminum High-Temperature Conductive Microporous Coating (Al-HTCMC) onto an aluminum surface. The coating consisted of aluminum particles brazed onto the aluminum surface, and it was concluded from evaporation experiments that the coating effectively improved wicking capabilities and that the system required almost zero superheat for evaporation to begin on the surface.

Since wicking structures are capable of aiding the heat transfer performance of a device, it is desired to optimize the wicking structure for maximum capillary evaporation. The main factor affecting heat transfer enhancement due to capillary evaporation is the particle size used in the fabrication of the wicking structure. The primary effect that particle size has on capillary evaporation is tied to the role that thin film evaporation plays within capillary evaporation. Comprehensive theoretical, experimental, and simulation studies have been conducted on the thin film evaporating region, and it is established that thin film evaporation greatly improves heat transfer performance during phase change heat transfer. Compared to the boiling heat transfer coefficient on the same surface, the heat transfer coefficient due to thin film evaporation is much higher overall. The reason for this largely stems from the vapor resistance to the liquid film in pool boiling systems. As vapor moves through the system, the liquid resists its flow. As a result, liquid thin film evaporation decreases the resistance to vapor flow since the liquid is evaporating, causing an enhancement to vapor flow and, therefore, heat transfer.

As shown in Figure 1, the thin film evaporation process for a sintered particle structure can be broken down into three distinct regions/processes: the meniscus film region, the evaporating thin film region, and the non-evaporating region. Within the thin film, a disjoining pressure is created, thus reducing the saturated vapor pressure and therefore causing easier evaporation and a more efficient heat transfer when heat is added to the thin film region. It is important to note that thin film evaporation isn't exclusive to sintered particles but other geometries and configurations as well.

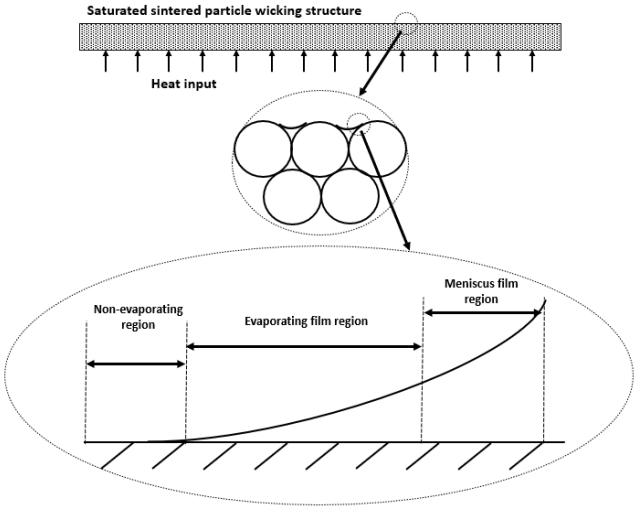

FIGURE 1: THIN FILM EVAPORATION IN SINTERED PARTICLES

Demsky and Ma [14] proposed a mathematical model to predict evaporation and fluid flow characteristics in the evaporating thin film region. The model predicted that thin film evaporation occurring on curved surfaces produces better heat flux distributions compared to flat surfaces. Kobayashi et al. [15] conducted theoretical and experimental studies on thin film evaporation at the meniscus edge in an evaporator. The studies were in agreement with each other and showed that large amounts of heat flux are transported through the thin film region. Ma et al. [16] developed a mathematical model for the evaporating thin film region by considering inertial force, disjoining pressure, surface tension, and curvature. It is determined the inertial force can be neglected, and a maximum velocity, curvature, and heat flux can be determined for optimal enhancement of heat transfer in the evaporating thin film. Nazari et al. [17] studied thin film evaporation in nanochannels and proposed a design for thermal management technologies. The design improved the momentum transport of the liquid, which is the limiting factor in steady-state capillary evaporation. The results showed unprecedented heat fluxes during steady-state conditions over an extended period of time.

As stated above, the enhancement can be done by introducing sintered particles to the inner wall of a heat pipe or other heat transfer device. As noted by Li and Joshi [18], the sintered particles act as a wicking structure, forcing capillary flow within the tube and also improving thin film evaporation. As seen in the zoomed-in portion of the sintered particles in Figure 1, there exists a thin film evaporating region between each set of sintered particles. As a result, the addition of the sintered particle wicking structure provides more nucleation sites for thin film evaporation to occur, thus improving overall capillary evaporation.

Wen et al. [19] conducted an examination of meniscus radii and determined it is not desirable to make the sintered particle size as small as possible in order to create the most nucleation sites for thin film evaporation to occur. Since the meniscus radius of the working fluid between two sintered particles is determined based on the size of sintered particles, the evaporating film region is greatly affected by the meniscus film region. Increasing the meniscus radius, i.e., increasing particle size, will cause the slope of the line in Figure 1 to increase, meaning more working fluid will exist in the thin film region. If there is too much-working fluid, the thin film becomes too large, and capillary evaporation becomes less efficient. Decreasing particle size, and thus the meniscus radius, means less fluid will be present in the thin film region. If there is not enough fluid in the thin film region, the working fluid will quickly evaporate, and dry out will occur.

When determining the sintered particle size to be used, liquid rewetting of the entire capillary structure must be examined. Liquid rewetting is important within capillary-driven flow because too much fluid will cause oversaturation of the sintered particle wicking structure and no thin film regions will exist, thus causing poor evaporation. If there is too little fluid within the wicking structure, the working fluid will evaporate too fast and burnout or hot spots will occur within the tube walls. As a result, selecting a sintered particle size that will allow for enough fluid flow through the wicking structure, while still maintaining evaporating thin films at nucleation sites is crucial to enhancing overall capillary evaporation [20].

However, nucleation sites not only promote thin film evaporation but also initiate the growth of bubbles. To determine the impact of bubble generation, the entire flow regime of a horizontal evaporation tube with a uniform cross-sectional area must be examined, like that shown in Figure 2. Fluid flow enters from the left and develops into various regimes as the fluid travels through the evaporation tube, where the heat transfer capability for each region is shown in the plot below the flow regimes. As fluid enters the pipe, nucleation sites produce bubbles that initiate bubbly flow. As more bubbles are formed, and further evaporation occurs, the bubbles begin to get bigger and join, producing slug flow within the tube. As slug flow develops, a continuous vapor space is created, and a thin layer of fluid separates the vapor from the tube wall, and annular flow is observed. As the annular flow develops, the thin film begins to evaporate, which is why a spike in the heat transfer coefficient is observed. As evaporation continues, dry-out conditions begin to occur, and annular flow transitions to mist flow – where the liquid is entrained within the vapor bubble space. Once the mist within the vapor bubble space evaporates, the vapor region becomes saturated.

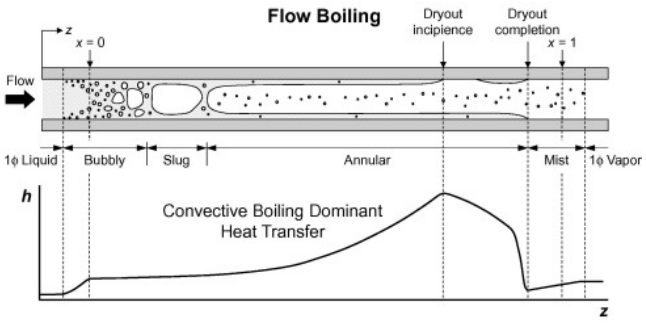

FIGURE 2: FLOW REGIME AND CONVECTIVE HEAT TRANSFER COEFFICIENTS FOR A HORIZONTAL TUBE WITH UNIFORM CIRCUMFERENTIAL HEATING [21].

According to the previous discussion, the addition of a sintered particle wicking structure could improve the overall heat transfer by coupling the capillary evaporation to thin-film evaporation. Adding sintered particles to the inner tube wall adds more nucleation sites for thin film evaporation to occur on the scale of the sintered particles. On the scale of the entire capillary tube, the sintered particles act as nucleation sites for bubble growth for overall fluid flow within the capillary tube. The bubbles formed at these nucleation sites will induce a bubbly regime that will develop into the annular regime, where thin film evaporation occurs. As a result, the addition of a wicking structure could significantly increase capillary evaporation due to the effectiveness of thin film evaporation in the flow regime and at the nucleation sites.

In this work, an experimental and theoretical investigation is performed to analyze the effect of sintered

copper particle wicking structure on the performance of a single evaporation tube at various heat inputs and inclination angles. The temperature profile across the evaporation tube is measured, and the effect of the radius of the particles is investigated theoretically. The results from this investigation will help to understand how the sintered particles can promote capillary evaporation and, therefore, boost the heat transfer coefficient. This effort will help design a novel low-temperature evaporator.

2. EXPERIMENTAL METHODS

To determine the meniscus radius effect on the saturation pressure, the experimental setup shown in FIGURE 3 was designed and built at the Multiphysics Energy Research Center (MERC) at the University of Missouri. The setup is comprised of four major components: a testing section, a reservoir, a condenser, and a collection tank. The testing section consists of a copper tube with an inner diameter of 14 mm and an outer diameter of 15 mm, a 0.5 mm thick layer of 105 μm sintered particles on the inner surface, and a flexible heater wrapped around the outer surface of the copper tube. A sintered particle plug was placed at the entrance region of the evaporation tube to ensure the flow of acetone is slow enough to enter the interior sintered structure rather than flow directly through the tube if there was no plug. A schematic of the cross-section of the evaporation tube and flow within can be observed in

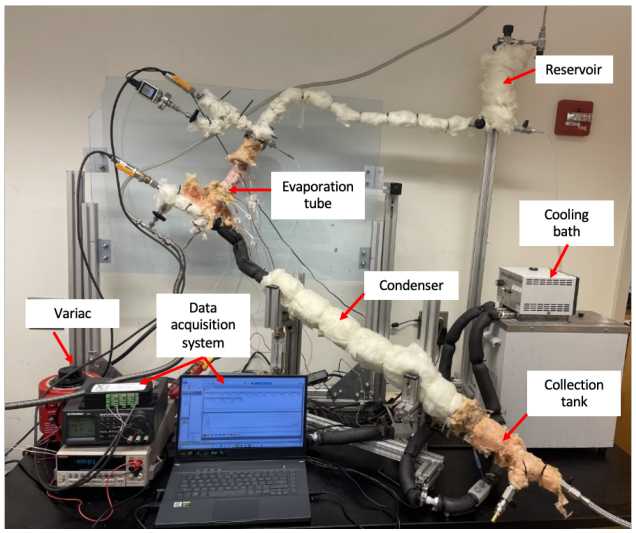

FIGURE 3: PHOTO OF THE EXPERIMENTAL SETUP

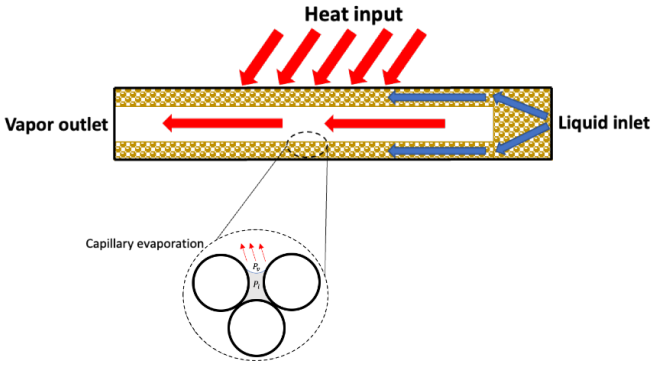

FIGURE 4: FLUID FLOW THROUGH THE EVAPORATION TUBE TEST SECTION.

The evaporation tube is the main component of the system, where the acetone evaporates, and temperature measurements are taken. To measure the temperature profile, 11 type-T thermocouples, with an accuracy of ± 0.5 °C, were equally spaced 1.42 cm apart along the outer surface of the evaporation tube. Small grooves were scored into the surface to ensure the thermocouples made good contact with the copper. The thermocouples were then secured using low-resistance thermal epoxy in addition to thermal tape. The epoxy was then used to secure a copper mesh over the thermocouples, and zip-ties were used to hold the mesh in place as the epoxy dried. The copper mesh was applied to ensure more uniform heating across the evaporation tube to minimize hot spots. The heating wrap was then placed around the entire tube and secured with thermal tape to ensure good contact. Finally, insulation and electrical tape were added to the evaporation tube to improve the insulation and hence reduce the heat losses.

The reservoir serves as the acetone supply while running the trials. Before trials are run, the reservoir is emptied, then charged with acetone. While conducting a trial, the acetone runs from the reservoir, through a hose, and into the single evaporation tube. As a result, it is vital that the bottom of the reservoir is located above the entrance of the single evaporation tube, so gravity can be utilized to promote fluid flow from the reservoir into the evaporation tube. The condenser was connected to a cooling bath that was kept at 15° C. As the evaporated acetone vapor leaves the evaporation tube and enters the condenser, the vapor is condensed back to liquid form within the condenser. Finally, a collection tank was connected to the end of the condenser to hold the acetone re-produced in the condenser.

TABLE 1: DIMENSIONS AND PARAMETERS FOR INVESTIGATED EVAPORATION TUBE.

Evaporation tube OD, d_e	15 mm
Evaporation tube ID, d_v	14 mm
Evaporator tube length, L_e	20 cm
Tube thickness, δ_e	0.5 mm
Evaporation tube material	Copper
Sintered particle material	Copper
Thermal conductivity of particles, k_s	400 W/m K
Wick thickness, δ_w	0.5 mm
Porosity of sintered particles, ε	0.5
Diameter of sintered particles, d_p	105 μm
Thermal conductivity of acetone, $k_{l,acetone}$	0.157 W/m K

2.1 Experimental Procedure

For the experimental procedure to occur, it is crucial that the single evaporation tube and the system can hold a vacuum. All experiments must be performed under a vacuum. Assuming the system is properly constructed with no air leaks, the experimental procedure is as follows:

1) Set the evaporation tube to the desired angle for experimentation.
2) Turn on the vacuum pump to begin evacuating the entire system of air.
3) Once vacuum conditions are reached, close the valve located on the top of the reservoir, which is connected to the vacuum pump.
4) Fill a beaker with 1000 ml of acetone.
5) Attach a hose to the bottom right side of the reservoir (the inlet), which is closed off with a ball valve.
6) Insert the other end of the hose into the beaker filled with 1000 ml of acetone and open the reservoir inlet ball valve. The vacuum that was created within the reservoir will create a suction effect and pull the acetone from the beaker into the reservoir.
7) Once it appears that no more acetone is being drawn into the reservoir, close the reservoir inlet ball valve. Measure the amount of acetone that is leftover, including the acetone that remains in the hose.
8) Briefly open the valve located at the top of the reservoir to remove any air that might have entered the reservoir during the charging process. Close the valve after the excess air has been removed.
9) Once closed, ensure the system is under vacuum conditions and close the valve that separates the vacuum pump from the entire system and turn the vacuum pump off.
10) Using the Variac connected to the heating wrap engulfing the evaporation tube, begin heating the evaporation tube. Allow for a five-minute pre-heating period.
11) Once pre-heated, open the valve located at the bottom left side of the reservoir (the outlet) to allow the charged acetone to begin flowing through the evaporation tube. Once the valve has been opened, begin a new temperature log.
12) Allow the system to run for 30 minutes uninterrupted. This constitutes one trial.
13) After 30 minutes, close the reservoir outlet valve and turn off the Variac. Collect the leftover acetone in the reservoir and measure how much acetone was used from the reservoir during the trial. Collect the acetone in the condenser and measure to see how much liquid was produced.
14) After data has been collected and fluids have been measured, repeat steps 2-14 for the next trial at a new power input.

For the purposes of this study, the above procedure was repeated for power inputs of 10, 30, 50, and 70 W. Trials were conducted for each of these power inputs at angles of -90°, -60°, -30°, 0°, 30°, 60°, and 90° as shown in FIGURE 5. It is important to note that when the evaporating tube is oriented at a negative angle, gravity aids in fluid flow. However, when the evaporation tube is oriented at positive angles, the fluid flow is more capillary driven since flow opposes the direction of gravity.

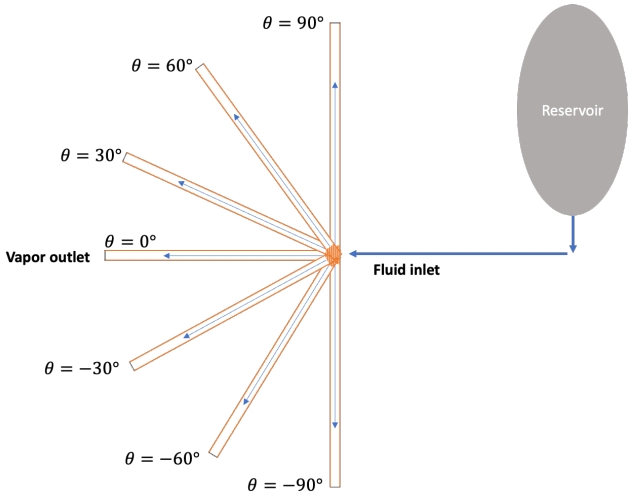

FIGURE 5: EXPERIMENTAL EVAPORATION TUBE POSITIONS AND THEIR CORRESPONDING INCLINATION ANGLES.

3. DATA ANALYSIS

The heating capacity of the heater and the cooling capacity of the condenser were calculated by:

$$\dot{Q}_{heater} = I \times V \quad (1)$$

and

$$\dot{Q}_c = \dot{m}_w c_p (T_{out} - T_{in}) \quad (2)$$

where I is the current, V is the voltage, $\dot{m}_w$ is the cooling water mass flow rate, T_{out} is the cooling water outlet temperature, and T_{in} is the cooling water inlet temperature. The voltage was measured using the Keithley 2701 digital multimeter with an accuracy of 4% in voltage and current [22].

An energy balance across the entire system was conducted for each trial to estimate heat losses. The power input into the heater was compared to the cooling capacity of the condenser and the difference was never found to exceed 6%, indicating the system was well insulated.

3.1 Repeatability Tests

To ensure the reliability of the experimental results, a few of the trials were repeated three times, and their measured temperature profiles and average steady-state temperatures were compared, as shown in FIGURE 6 and FIGURE 7, respectively. From these results, the largest percent difference in average temperatures was 4.09%, which was between trials 1 and trial 2, indicating the reliability and repeatability of the results obtained from this experimental investigation.

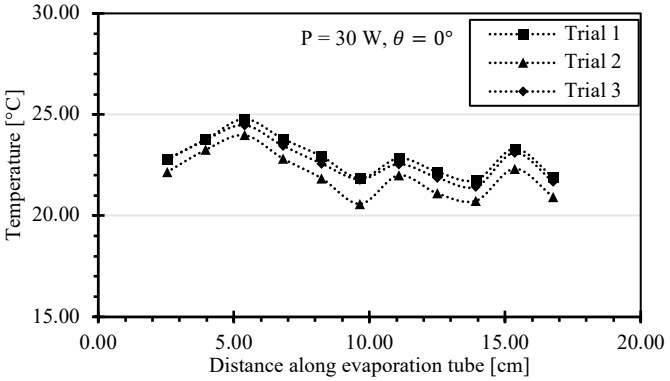

FIGURE 6: TEMPERATURE DISTRIBUTION ALONG EVAPORATION TUBE FOR THREE TRIALS AT A POWER INPUT OF 30 W AND AN INCLINATION ANGLE OF 0°

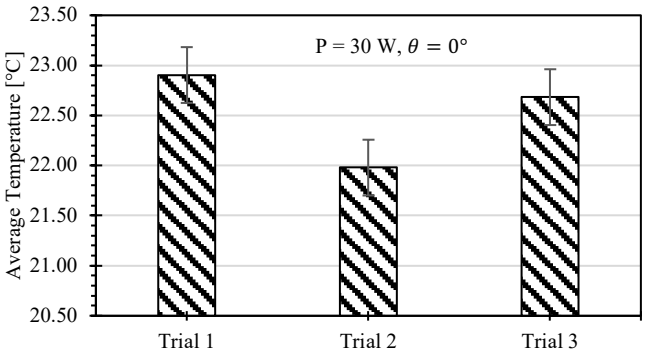

FIGURE 7: AVERAGE STEADY STATE TEMPERATURE FOR THREE REPEATED TRIALS AT A POWER INPUT OF 30 W AND AN INCLINATION ANGLE OF 0°

4. RESULTS AND DISCUSSION

The temperature profiles along the evaporation tube are presented for various power inputs and inclination angles to examine the effects of these factors on the performance of the evaporation tube. In addition to this, the inlet and outlet temperatures of the working fluid were measured.

4.1 Experimental Results

4.1.1 Effect of Tilt Angle

The heat input into the evaporation tube came from a heating wrap connected to a Variac. FIGURE **8:** 8 depicts the effect the tilt angle has on the temperature profile on the evaporation tube for a 30 W power input. The corresponding average temperatures for each trial can be observed in Figure 9. From FIGURE 5, it can be observed that for each corresponding opposite angle, the positive appeared to result in larger surface temperatures. For example, for the tilt angles of -60° and 60°, 60° was found to result in higher surface temperatures. This trend is further backed up by the results of the average steady-state temperatures in Figure 9. For the inclination angles of -30° and 30°, the average steady-state temperatures were 26.89 °C and 27.41 °C, respectively.

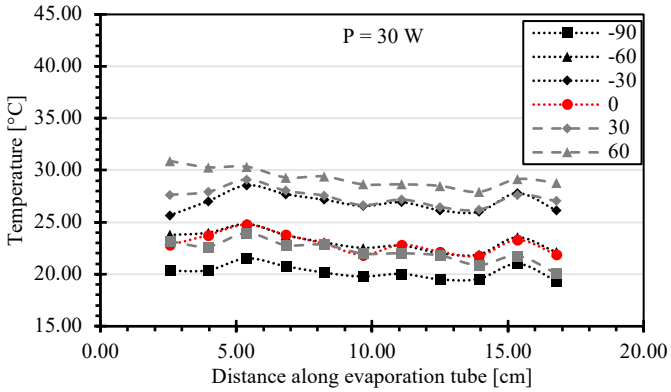

FIGURE 8: TEMPERATURE PROFILE ALONG EVAPORATION TUBE FOR A 30 W POWER INPUT AT -90°, -60°, -30°, 0°, 30°, 60°, AND 90°.

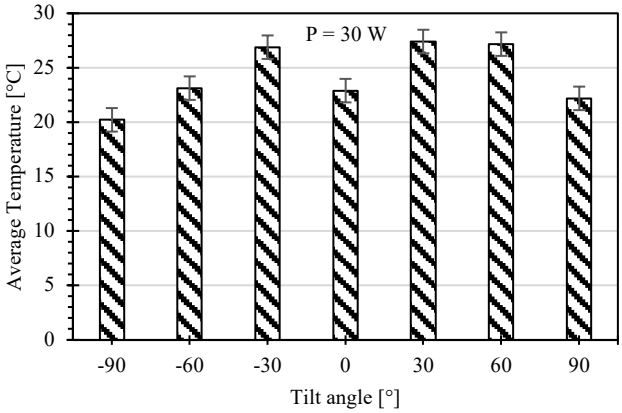

FIGURE 9: AVERAGE TEMPERATURE ALONG THE EVAPORATION TUBE FOR A 30 W POWER INPUT

One potential explanation for this is due to the effect of gravity when the evaporation tube is in a negative angle orientation, where the inlet is higher than the outlet. The primary force driving the fluid through the sintered particle wicking structures is capillary force. However, when oriented at a negative angle, the force of gravity is also playing a role which could result in more fluid passing through the tube, thus leading to lower surface temperatures. The results found in Figure 10 which provide a comparison between the total amount of fluid collected in the collection tank for each opposite angle, help to support this theory. On average, the negative angles were observed to produce 60.33 ml more fluid than the positive angles, with the difference between -90°/90° being the largest at 86 ml. It is interesting to note that the angles of -60° and 60° produced the most amount of fluid.

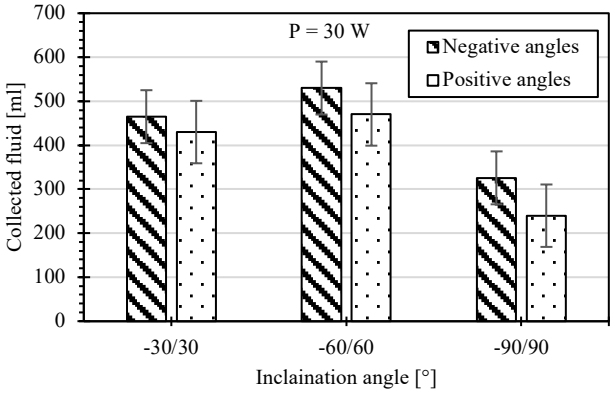

FIGURE 10: FLUID COLLECTED FROM THE COLLECTION TANK AFTER 30-MINUTE TRIAL.

It can also be observed in Figure 9 that the temperature profile along the evaporation tube for all trials was downward sloping, or in other words, the temperature appeared to reduce as the fluid traveled further along the tube. To investigate this trend the inlet and outlet temperatures were compared for each inclination angle for a power input of 30 W, and the results can be observed in Figure 11. As seen in Figure 11, the fluid inlet temperature was always observed to be larger than the outlet temperature, with no exceptions. Another interesting observation that can be made is that larger inclination angles resulted in larger fluid inlet temperatures and consequentially larger outlet temperatures as well. As with the results shown in Figure 9 for the average temperatures, this can also be due to the effect of gravity. The larger the tilt angle, the more the fluid will have to work against gravity. Therefore, the contact time between the fluid and the wall of the inner wall is greater, thus resulting in the fluid being heated to a higher temperature. Similarly, as the results in Figure 10, less fluid is passing through the evaporation tube for larger inclination angles, and therefore, the fluid will be able to reach higher temperatures at the same heat inputs.

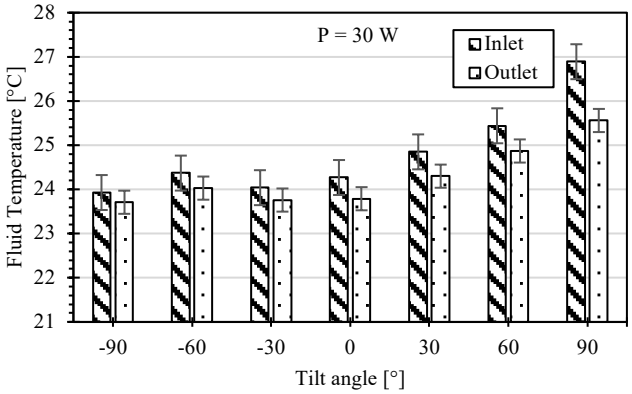

FIGURE 11: INLET AND OUTLET TEMPERATURES FOR WORKING FLUID FOR A 30 W POWER INPUT

4.1.2 Effect of Power Input

The performance of the evaporation tube was tested at power inputs of 10, 30, 50, and 70 W for each tilt angle. The temperature distribution along the evaporation tube for all heat inputs at a 60° tilt angle can be observed in Figure 12. As would be expected, a larger heat input was typically found to result in larger surface temperatures, as shown by the average temperatures in Figure 13. As with the results shown in Figure 8, the temperature distributions in Figure 12 are all downward sloping. However, the slope appears to be more negative for larger power inputs as opposed to the results in Figure 8, where all trials were for the same 30 W power input, and only the tilt angle was changing. For those trials, the slopes appeared to be very similar, and the temperature distributions followed the same trend. The temperatures distributions for tilt angles -90°, -60°, -30°, 30°, 60°, and 90° for power inputs of 50 W and 70 W were plotted to see if this trend is consistent for other power inputs, and those can be observed in Figure 14 and Figure 15, respectively. From those results, as with the 30 W power input, the temperature distributions for the 50 W and 70 W all appeared to follow similar trends for each tilt angle, with the only main difference being the average temperatures which followed the same trend described in FIGURE 9.

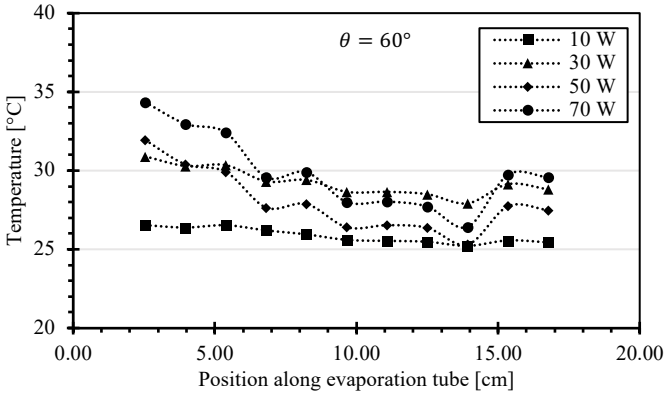

FIGURE 12: TEMPERATURE PROFILE ALONG EVAPORATION TUBE AT 60° FOR POWER INPUTS OF 10, 30, 50, AND 70 W.

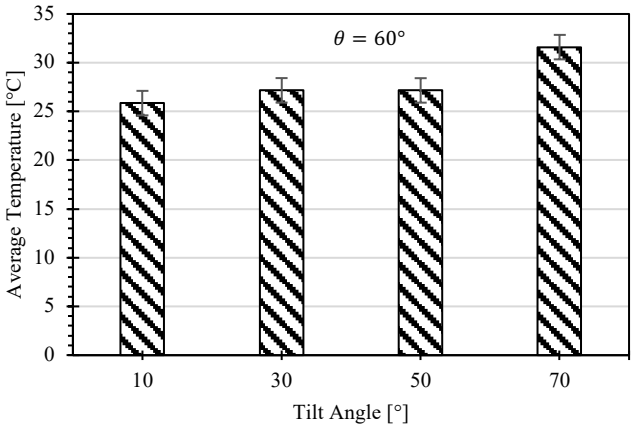

FIGURE 13: AVERAGE STEADY STATE TEMPERATURE FOR A 60° TILT ANGLE AT POWER INPUTS OF 10, 30, 50, AND 70 W.

From Figure 12, the temperature readings from 2–8 cm along the evaporation tube make sense, meaning the higher power inputs resulted in higher temperatures. However, at some point between 8-10 cm, the temperature for the 70 W power input was observed to drop below that of the 50 W power input. It wasn't until around 15 cm where a sharp increase in the temperature of the 70 W mark was observed, and it returned above that of the 50 W. A temperature increase was observed at this location for all power inputs, however, the jump was much more significant at 70 W. As can be seen in Figure 15, this pronounced temperature jump was observed for all tilt angles. This temperature increase could be due to a dryout condition, where all the fluid had been fully evaporated and therefore resulting in higher surface temperatures near the outlet.

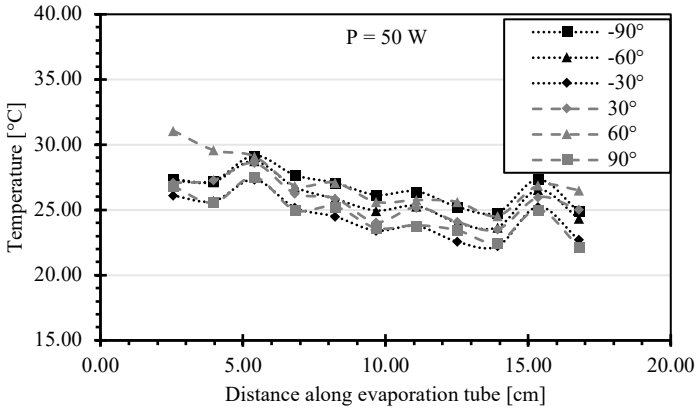

FIGURE 14: TEMPERATURE PROFILE ALONG EVAPORATION TUBE FOR A 50 W POWER INPUT AT -90°, -60°, -30°, 30°, 60°, AND 90°.

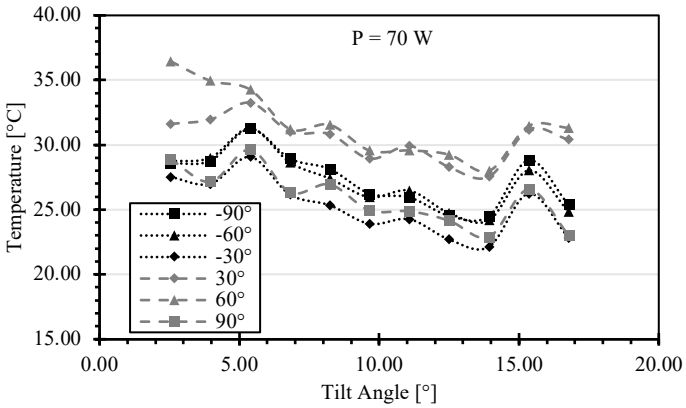

FIGURE 15: TEMPERATURE PROFILE ALONG EVAPORATION TUBE FOR A 70 W POWER INPUT AT -90°, -60°, -30°, 30°, 60°, AND 90°.

The average steady-state temperatures for tilt angles -90°, -60°, -30°, 30°, 60°, and 90° for power inputs of 30 W, 50 W, and 70 W, can be observed in Figure 16. As would be expected, for almost all tilt angles, the larger power inputs resulted in larger average temperatures. The only exceptions to this occurred at -30° and 30°, where for both cases, the 30 W power input resulted in a larger average surface temperature when compared to both 50 W and 70 W at -30°, and 50 W when at 30°. In addition to this, a tilt angle of 90° was observed to result in the lowest average surface temperatures except for 30 W, where it was the second lowest, with -90° being the lowest.

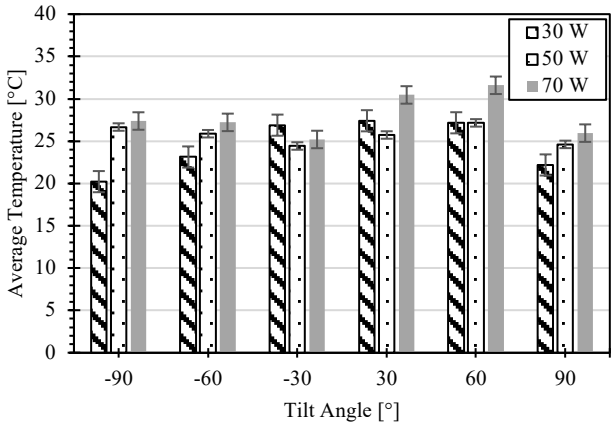

FIGURE 16: AVERAGE TEMPERATURE ALONG EVAPORATION TUBE FOR A 30, 50, AND 70 W POWER INPUT

4.2 Theoretical Results

4.2.1 Effect of Particle Radius

Using the experimental results described below, the effect of the radius of the sintered particles on the temperature distribution is determined from [23]

$$P_v = P_l - \frac{2\sigma}{0.654 r_p} \tag{3}$$

where P_v is the theoretical pressure drop of the vapor, P_l is the experimentally measured pressure of the liquid, σ is the surface tension and r_p is the radius of the sintered particle.

The 0.654 coefficient in Eq. 3 represents a hexagonal arrangement of the sintered wick particles, the most common formation produced when manufacturing wicking structures from sintered particles. P_l was able to be attained from the measured temperatures at each state point by converting them to the corresponding pressure assuming the fluid is in a saturated state. The diameter of the particles chosen for analysis were 5, 10, 50, 100, and 150 µm. From the results shown in Figure 17, the radius of the particle has a clear effect on the temperature distribution along the evaporation tube. It is found that larger particle sizes resulted in larger pressure drops and, therefore, larger temperatures at each point along the evaporation tube. The red line represents the results that were experimentally measured, and it was found to match closely with a particle size of 150 µm.

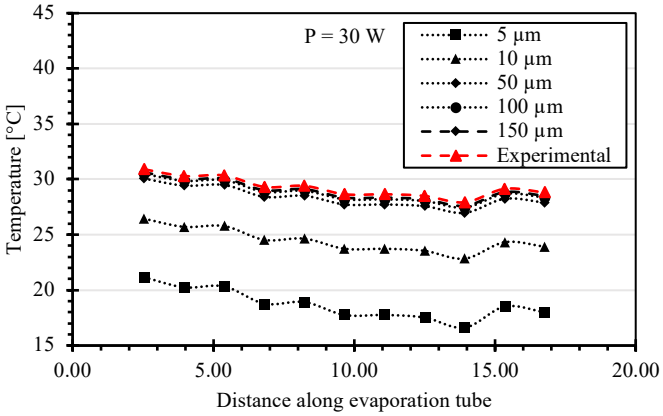

FIGURE 17: PARTICLE RADIUS EFFECT ON TEMPERATURE DISTRIBUTION

5. CONCLUSION

A wicking structure created from sintered copper particles was added to inner surface of a copper evaporation tube. Experimental studies were conducted to study the effect of the sintered particles on the surface temperature profile of the evaporation tube at heating power inputs of 10, 30, 50, and 70 W and inclination angle ranging from -90° to 90°, with acetone acting as the working fluid. The results from the experimental investigation showed that inclination angles of -30° and 30° resulted in the largest average surface temperatures, whereas experimental studies conducted at inclination angles of -60° and 60° produced more condensate. The power input into the evaporation tube was found to have a greater effect on the temperature distribution along the evaporation tube compared to the inclination angle. For all trials, inlet temperature of the fluid was found to be higher than the outlet temperature of the vapor. Similarly, the temperature distribution along the evaporation tube was always observed to be downwards sloping, with larger power inputs resulting in a steeper slope and at some location the outlet temperature of the fluid was found to be lower than the surface temperature indicating the effect of capillary evaporation. The theoretical results showed that the radius of the particle has a clear effect on the performance of the evaporation tube. Larger particle sizes with diameters of 50, 100, and 150 µm yielded larger pressure drops and, coincidentally, larger surface temperatures. In future work, these results will be validated experimentally.

ACKNOWLEDGEMENTS

This material is based upon work supported by the U.S. Department of Energy, Office of Science, Building Technologies Office. This research used resources of the Building Technologies Research and Integration Center (BTRIC) of the Oak Ridge National Laboratory, which is a DOE Office of Science User Facility.

Declaration of Competing Interests

The authors state that they have no known competing financial interests or personal relationships that could have influenced the work reported in this paper.

REFERENCES

[1] Bigham S, Fazeli A, Moghaddam S. Physics of microstructures enhancement of thin film evaporation heat transfer in microchannels flow boiling OPEN 2017. https://doi.org/10.1038/srep44745.

[2] Bigham S, Moghaddam S. Microscale study of mechanisms of heat transfer during flow boiling in a microchannel. Int J Heat Mass Transf 2015;88:111–21. https://doi.org/10.1016/J.IJHEATMASSTRANSFER.2015.04.034.

[3] Bigham S, Moghaddam S. Role of bubble growth dynamics on microscale heat transfer events in microchannel flow boiling process. Appl Phys Lett 2015;107:244103. https://doi.org/10.1063/1.4937568.

[4] Palko JW, Lee H, Agonafer DD, Zhang C, Jung KW, Moss J, et al. High heat flux two-phase cooling of electronics with integrated diamond/porous copper heat sinks and microfluidic coolant supply. Proceedings of the 15th InterSociety Conference on Thermal and Thermomechanical Phenomena in Electronic Systems, ITherm 2016 2016:1511–7. https://doi.org/10.1109/ITHERM.2016.7517728.

[5] Plawsky JL, Fedorov AG, Garimella S v, Ma HB, Maroo SC, Chen L, et al. Nano-and Microstructures for Thin-Film Evaporation-A Review 2014. https://doi.org/10.1080/15567265.2013.878419.

[6] Thome JR. Boiling in microchannels: a review of experiment and theory. Int J Heat Fluid Flow 2004;25:128–39. https://doi.org/10.1016/J.IJHEATFLUIDFLOW.2003.11.005.

[7] Xu J, Gan Y, Zhang D, Li X. Microscale boiling heat transfer in a micro-timescale at high heat fluxes. J

Micromech Microeng 2005;15:362–76. https://doi.org/10.1088/0960-1317/15/2/017.

[8] Wang Y, Wang P, Wang N, Pan Y, Xu J, Shen S, et al. Transient flow pattern based microscale boiling heat transfer mechanisms. INSTITUTE OF PHYSICS PUBLISHING JOURNAL OF MICROMECHANICS AND MICROENGINEERING J Micromech Microeng 2005;15:1344–61. https://doi.org/10.1088/0960-1317/15/6/028.

[9] Dupont V, Thome JR, Jacobi AM. Heat transfer model for evaporation in microchannels. Part II: comparison with the database. Int J Heat Mass Transf 2004;47:3387–401. https://doi.org/10.1016/J.IJHEATMASSTRANSFER.2004.01.007.

[10] Kandlikar SG, Widger T, Kalani A, Mejia V. Enhanced flow boiling over open microchannels with uniform and tapered gap manifolds. J Heat Transfer 2013;135. https://doi.org/10.1115/1.4023574/367147.

[11] Dai X, Yang F, Yang R, Lee Y-C, Li C. Micromembrane-enhanced capillary evaporation 2013. https://doi.org/10.1016/j.ijheatmasstransfer.2013.05.030

[12] Zhang C, Yu F, Li X, Chen Y. Gravity–capillary evaporation regimes in microgrooves. AIChE Journal 2019;65:1119–25. https://doi.org/10.1002/AIC.16484.

[13] Wang X, Fadda D, Godinez JC, Lee J, You SM. Capillary evaporation of water from aluminum high-temperature conductive microporous coating. Int J Heat Mass Transf 2020;153. https://doi.org/10.1016/J.IJHEATMASSTRANSFER.2020.119660.

[14] Demsky SM, Ma HB. THIN FILM EVAPORATION ON A CURVED SURFACE 2010. https://doi.org/10.1080/10893950490477590.

[15] Kobayashi Y, Ikeda S, Iwasa M. Evaporative heat transfer at the evaporative section of a grooved heat pipe. Https://DoiOrg/102514/3756 2012;10:83–9. https://doi.org/10.2514/3.756.

[16] Ma HB, Cheng AP, Borgmeyer AB, Wang AYX. Fluid flow and heat transfer in the evaporating thin film region n.d. https://doi.org/10.1007/s10404-007-0172-5.

[17] Nazari M, Gorman M, Ghasemi H. Unprecedented capillary evaporative heat flux in nanochannels. InterSociety Conference on Thermal and Thermomechanical Phenomena in Electronic Systems, ITHERM 2019;2019-May:329–34. https://doi.org/10.1109/ITHERM.2019.8757337.

[18] Li W, Joshi Y. Capillary-Assisted Evaporation/Boiling in PDMS Microchannel Integrated with Wicking Microstructures. Langmuir 2020;36:12143–9. https://doi.org/10.1021/ACS.LANGMUIR.0C01711/SUPPL_FILE/LA0C01711_SI_001.PDF.

[19] Wen R, Xu S, Lee Y-C, Yang R. Capillary-Driven Liquid Film Boiling Heat Transfer on Hybrid Mesh Wicking Structures 2018.

[20] Farokhnia N, Irajizad P, Sajadi SM, Ghasemi H. Rational Micro/Nanostructuring for Thin-Film Evaporation. Journal of Physical Chemistry C 2016;120:8742–50. https://doi.org/10.1021/ACS.JPCC.6B01362/SUPPL_FILE/JP6B01362_SI_001.PDF.

[21] Kim SM, Mudawar I. Review of databases and predictive methods for heat transfer in condensing and boiling mini/micro-channel flows. Int J Heat Mass Transf 2014;77:627–52. https://doi.org/10.1016/J.IJHEATMASSTRANSFER.2014.05.036.

[22] Keithley 2010 Series: 7.5 Digit Multimeter with Scanning | Tektronix n.d. https://www.tek.com/en/products/keithley/digital-multimeter (accessed July 26, 2022).

[23] Ma H. Oscillating heat pipes. 2015. https://doi.org/10.1007/978-1-4939-2504-9.